Intense 2.7 mu m emission of Er3+/Pr3+ doped Ga5Ge20Sb10S65 chalcogenide glass

Quan Liu, Yinsheng Xu, Qi Xia, Weiwei Li, Xianghua Zhang

Intense 2.7 μm emission of Er^{3+}/Pr^{3+} doped $Ga_5Ge_{20}Sb_{10}S_{65}$ chalcogenide glass

Quan Liu[1], Yinsheng Xu[1,*], Qi Xia[2,*], Weiwei Li[3], Xianghua Zhang[1,4]

State Key Laboratory of Silicate Materials for Architectures, Wuhan University of Technology, Wuhan 430070, China

School of Intelligent Manufacturing and Electronic Engineering, Wenzhou University of Technology, Wenzhou 325035, China

State Key Laboratory of Advanced Technology for Materials Synthesis and Processing, Wuhan University of Technology, Wuhan 430070, China

Institut Des Sciences Chimiques de Rennes UMR 6226, CNRS, Université de Rennes 1, Rennes 35042, France

E-mail: xuyinsheng@whut.edu.cn (Y. X.), xia65462969@163.com (Q. X.)

Abstract:

There are numerous vital usages for mid-infrared lasers in satellite communication, biomedicine, military, remote sensing, and environmental monitoring. In this work, a progression of Er^{3+} ions doped, Er^{3+}/Pr^{3+} ions co-doped $Ga_5Ge_{20}Sb_{10}S_{65}$ glasses were prepared, and their physical performances and structural characteristics were examined. To understand the non-phonon-assisted energy transfer mechanism, we recorded the up-conversion and infrared fluorescence emission spectra by pumping with a commercial 980 nm LD. Then the 2.7 μm strong fluorescence signal intensity can be obtained when the doped concentration of Pr^{3+} is proper. After the doping of Pr^{3+}, fluorescence lifetime results

This article has been accepted for publication and undergone full peer review but has not been through the copyediting, typesetting, pagination and proofreading process, which may lead to differences between this version and the Version of Record. Please cite this article as doi: 10.1111/jace.19181.

revealed that the lifetimes of the Er^{3+}: $^4I_{13/2}$ level fell dramatically from 7.33 to 1.90 ms, which experienced a much more significant decrease in lifetimes than the Er^{3+}:$^4I_{11/2}$ level. The mid-infrared fluorescence performances were assessed by the determined J-O parameters and relative emission cross-sections. Additionally, the generally huge emission cross-sections and the small pump energy show that it is possible to obtain population inversion with relatively small pump energy, thus the Er^{3+}/Pr^{3+} glasses have great potential to be 2.7 μm laser materials.

Keywords:

Chalcogenide glass; Er^{3+}/Pr^{3+} co-doped; $Ga_5Ge_{20}Sb_{10}S_{65}$ glass; 2.7 μm emission;

1. Introduction

Recently, mid-infrared (MIR) lasers about 3 μm certainly stand out enough to be noticed owing to their various useful application, for example, military countermeasures, remote detecting, environment contamination checking, satellite correspondence, and clinical medical procedure[1-5]. According to previous studies, Er^{3+} is a good candidate material for 2.7 μm MIR emission due to its radiative transition of $^4I_{11/2}\rightarrow{}^4I_{13/2}$. Additionally, with a 980 nm business laser, Er^{3+} tends to be easily pumped[6-8]. However, it is as yet a critical difficulty to get the productive 2.7 μm emission because of the self-terminating issue, thus the $^4I_{13/2}$ level has a larger lifetime than the $^4I_{11/2}$ level. Through energy transfer (ET), Pr^{3+}, Ho^{3+}, Yb^{3+}, and Tm^{3+} have been added as sensitizers to extinguish the Er^{3+}: $^4I_{13/2}$ level, which helps solve the issue of self-terminating.

Given that the non-phonon-assisted ET process is a more effective way of quenching the electrons of $^4I_{13/2}$ levels compared with the phonon-helped one. The energy levels between Er^{3+} and Pr^{3+} are relatively close, and energy transfer can occur. This ET process does not need to be accompanied by the absorption or emission of phonons, nor does it need to use photons as a medium. Therefore, the ET efficiency of non-phonon-assisted ET processes is higher than that of phonon-assisted ET. Therefore,

Pr^{3+} ions can suppress the adverse effects mentioned above and can realize the possibility to achieve population inversion.

Up to now, numerous work have concentrated on Er^{3+}/Pr^{3+} co-doped glasses, mainly including fluoride glass[9], oxyfluorotellurite glass[10], fluorophosphate glass[11], tellurite glasses[12], piezoelectric ceramic[13], and crystals[14, 15]. Nevertheless, the relatively high phonon energy in those matrix glasses can suppress mid-infrared fluorescence output. Chalcogenide glasses are considered to be suitable mid-infrared fluorescent materials owing to their advantages of low phonon energy, wide transmission range, and high refractive index[16, 17], so they can exhibit low non-radiation transition rate and large emission cross-section[18, 19].

The $Ga_5Ge_{20}Sb_{10}S_{65}$ (GGSS) glass is chosen as the matrix doped with Er^{3+} and Pr^{3+} for enabling efficient fluorescence. This glass is suitable for drawing into optical fiber owing to its good thermal stability against crystallization and excellent thermo-mechanical properties[20, 21]. Furthermore, because of the presence of Ga element, this glass sample has a high solubility of RE ions, so it helps to obtain intense MIR emission[22, 23]. In this paper, Er^{3+} and Pr^{3+} doped samples in various concentrations were fabricated, and their basic physical properties and structural characteristics were investigated. Pumping by a 980 nm LD, the fluorescence spectra of the visible and infrared range were measured, and the ET principle for Er^{3+} and Pr^{3+} co-doped GGSS samples was investigated. In addition, the relative J-O parameters, radiative parameters, emission cross-sections, and gain coefficients were all calculated. The enhanced fluorescence emission and a relatively large value of emission cross-sections show that the Er^{3+}/Pr^{3+} co-doped GGSS glasses are promising materials to realize strong 2.7 μm emission.

2. Experimental

2.1 Glass preparation

A series of $Ga_5Ge_{20}Sb_{10}S_{65}$-$x$$Er^{3+}$/$y$$Pr^{3+}$ (x = 0, 0.05, 0.1, 0.2, 0.3. 0.4, y = 0.05, 0.1, 0.2, in mol%) chalcogenide glasses were prepared through melt quenching method. Firstly, high-purity raw element

materials (Ga, Ge, Sb, S, 5N) and rare-earth sulfides (Pr_2S_3, Er_2S_3, 3N) were all weighed in the glove box loaded up with N_2. Afterward, they were put into a quartz ampoule which is pre-cleaned. Under a vacuum of 10^{-3} Pa, the ampoule was heated to 120 °C for about 2 hours to remove the water on the surface of the glass tube, then sealed with an oxyhydrogen flame gun. Next, the ampoule was homogenized by melting it at 950 °C for 14 hours, followed by quenching and 2 hours of annealing at a temperature ($T = T_g$ - 20 °C). Finally, the glass rod was cut to the right dimensions (10 mm diameter, 2 mm thickness) and then was polished to achieve a mirror effect to meet the measurement requirements.

2.2 Measurement

A differential scanning calorimeter method (DSC, STA449F1, NETZSCH, Berlin, Germany) was used to measure the T_g. A glass fragment weighing approximately 15 mg was placed inside an aluminum pan for measurement. On an X-ray diffractometer (D8 Discover, Bruker, Karlsruhe, Germany), XRD measurements of the powder sample were made in the 2θ range of 10–80°. Using a balance as well as a density measurement kit, the Archimedes principle was used to quantify the densities of several types of glass. An infrared variable angle spectroscopy ellipsometer (IR-VASE Mark II, J.A. Woollam, Lincoln, NE, USA) is used to measure the refractive indices (n) of 1.7–20 μm. In 100-500 cm^{-1}, a Raman spectrometer equipped with a 633 nm laser excitation (LabRam HR Evolution, Horiba Jobin Yvon, Paris, France) was employed to collect Raman spectra. UV-Vis-NIR spectrophotometer (Lambda 900, Perkin-Elmer, Waltham, MA, USA) was used to detect the optical absorption spectra between 600-2500 nm with an error of ±1 nm. Using a Fourier transformed-IR spectrometer (FTIR; INVENIO S, Bruker, Ettlingen, Germany), the transmittance and absorbance spectra of glass samples were determined in 2-25 μm.

The fluorescence spectra were obtained by using a fluorescence spectrometer (FLS980, Edinburgh Instruments, UK) in conjunction with an InSb detector (1.3-3.0 μm) and R928P PMT (450-750 nm), which was equipped with a 980 nm LD. Fluorescence decay curves were captured using a digital oscilloscope (TDS3012C, Tektronix) and signal generator (TDS3051C, Tektronix). To guarantee the

comparability of the obtained fluorescence intensities, all testing variables (pump power and sample location) were maintained at a consistent level.

3 Results and Discussion

3.1 Physical properties

XRD patterns of GGSS-xEr^{3+} (x = 0.05, 0.1, 0.2, 0.3, 0.4, mol%) glass samples are shown in **Fig. 1 (a)**. The results show two broad diffraction peaks and no obvious crystal phase when the Er^{3+} ion concentration gradually grows from 0.05 to 0.4 mol%, indicating that all the samples are in a uniform amorphous state without crystallization. The DSC curve of matrix glass without RE ions doped is shown in **Fig. 1 (b)**. The T_g of the GGSS glass is about 300 °C, which is similar to the result of Ref. [24]. No obvious crystallization peaks exist, indicating the good thermal resistance to crystallization of GGSS glass and its appropriateness for drawing optical fiber. As shown in **Fig. 1 (c)**, the max value of infrared transmittance exceeds 70% during 2-12 μm for the matrix glass, covering the emission range of Er^{3+} at 2.7 μm. The absorption bands at about 2.8 μm and 4.1 μm are according to stretch modes of -OH and S–H vibrations, respectively, and the band at 9.2 μm belongs to Sb–O bond vibration. From the inset, there are no visible impurity particles in this glass, presenting a relatively transparent observation. The refractive indices in the 2-12 μm are shown in **Fig. 1 (d)**. Theoretically, a large refractive index value can provide high spontaneous emission feasibility and a big emission cross-section of 10^{-20} cm^2 in our previous work[25]. As the plot shows, the density marginally rose from 3.222 to 3.241 g/cm^3 when the Pr^{3+} concentration increased.

Given that the Raman spectrum is an effective tool for figuring out the structure of glass that affects the fluorescence performance of the glasses, the deconvolution of the Raman spectrum based on "Gaussian multipeak fitting" is presented in **Fig. 2**. In the case of $Ga_5Ge_{20}Sb_{10}S_{65}$ glass, it can meet the stoichiometric ratio condition and its glass network structure mainly includes [GeS_4], [GaS_4] tetrahedra, and [SbS_3] trigonal pyramids[26]. A major broad band is observed from 200 to 450 cm^{-1} in the Raman spectrum that is formed by overlapping multiple frequency bands, such as at 342 cm^{-1} is the [$GeS_{4/2}$]

tetrahedral v_1 (A_1) stretched vibration mode[27], and at 314 cm^{-1} is the [$GaS_{4/2}$] tetrahedra stretched vibration mode. There are two shoulders at 292 cm^{-1} and 370 cm^{-1}, one due to the stretched vibration mode of [$SbS_{3/2}$] trigonal pyramid units and the other due to the Ge-S bonds companion vibration mode[28, 29]. At 269 cm^{-1}, there is a small band which is due to S_3(Ge)Ga–Ga(Ge)S_3 homopolar bonds[30], and at 430 cm^{-1} the corners connected [$GeS_{4/2}$] cause a band to appear[31]. The small peak in 140-150 cm^{-1} is owing to the distortion mode of [$GeS_{4/2}$] tetrahedra[32]. This glass will have fewer defects because it is consistent with the stoichiometric ratio, which favors the consistent distribution of RE ions and the decline of defect absorption energy, thus the fluorescence emission will be increased[33]. It should be pointed out that this glass shows low phonon energy, which is advantageous for reducing the multi-phonon relaxation of excited states, thus obtaining improved MIR emission in these glasses. When the doping concentration of RE ions is relatively low, there is no obvious change in the Raman spectra for different Er^{3+} and Pr^{3+} concentration doped glass samples.

3.2 Absorption spectra and relative J-O theory analysis

As shown in **Fig. 3 (a)**, the absorption spectra of GGSS-$x$$Er^{3+}$ (x = 0.05, 0.1, 0.2, 0.3, 0.4, mol%) glass samples are presented. As marked in the figure, four typical absorption bands focus on 658, 804, 979, and 1535 nm, matching the transitions from $^4I_{15/2}$ to $^4F_{9/2}$, $^4I_{9/2}$, $^4I_{11/2,}$ and $^4I_{13/2}$. According to the $^4I_{15/2}\rightarrow{}^4I_{11/2}$ strong ground absorption band, it can be inferred that a 980 nm laser can effectively pump Er^{3+} doped GGSS glass. The inset of Fig. 3(b) shows that when the Er^{3+} ions concentration rises, the integral absorption intensity of $^4I_{15/2}\rightarrow{}^4I_{11/2}$ (980 nm) increases linearly, indicating that this glass matrix has a uniform distribution of Er^{3+} ions.

As presented in **Fig. 3 (c)**, the absorption spectra of the Er^{3+} ions doped, Pr^{3+} ions doped, Er^{3+}/Pr^{3+} ions co-doped GGSS glass samples from 600 to 3000 nm are recorded. For Pr^{3+} doped sample, three transitions from ground state level $^3H_4$ to upper energy levels are observed at wavelengths of ~1484 nm ($^3F_4$), ~1596 nm ($^3F_3$), and ~2040 nm ($^3F_2$). For Er^{3+}/Pr^{3+} co-doped sample, there is absorption band

overlap occurring at 1537 cm^{-1}, which ascribes to Er^{3+}: $^4I_{13/2}$ and Pr^{3+}: $^3F_4$, $^3F_3$ level, so it may occur ET between these two RE ions according to ET theory developed by Foster–Dexter[34, 35], which will be further discussed below.

Utilizing the Judd-Ofelt (J-O) theory, observed absorption spectra were applied to analyze the radiative characteristics[36, 37]. For the GGSS-0.2Er^{3+} glass, **Table 1** lists the oscillator strengths from the lower level ($^4I_{15/2}$) to the higher level. It is obvious that the values of f_{exp} and f_{cal} are relatively close.

The least-square method[38] was utilized to fit the theoretical and experimental oscillator strengths to produce the relative J-O intensity parameters Ω_t (t = 2, 4, 6). Related J-O parameters had been determined using a conventional computation of matrix elements which is reported by Tanabe *et al*.[39]. For GGSS-0.2Er^{3+} glass sample, $\Omega_2 = 8.62\times10^{-20}$ cm^2, $\Omega_4 = 2.44\times10^{-20}$ cm^2, $\Omega_6 = 1.72\times10^{-20}$ cm^2, which are comparable to similar chalcogenide glasses[40], and its root-mean-square (RMS) is 2.78×10^{-6}, demonstrating the validity of the results. Ω_2 is influenced by the symmetry of the coordination environment of RE ions as well as the covalence of the negative coordination ions[41], while Ω_4 and Ω_6 are influenced by viscosity, rigidity, and dielectric property of the bulk glass, and the vibronic transitions also have an impact on these parameters. As is shown in **Table 2**, for GGSS-0.2Er^{3+} glass, the value of Ω_2 is rather bigger than that of ZBYA glass (3.74×10^{-20} cm^2), oxyfluorotellurite glass (5.40×10^{-20} cm^2), fluorophosphate glass (5.14×10^{-20} cm^2), and tellurite glass (4.79×10^{-20} cm^2), indicating this glass owns strong covalence and low symmetry. The high value of Ω_4/Ω_6 = 1.42 would benefit the stimulated emission in a laser-active substance, thus implying a strong mid-infrared emission[42].

For GGSS-0.2Er^{3+} glass, fluorescence transition characteristics are shown in **Table 3** using related calculation formula[46, 47]. The electrical dipole transition probability A_{rad} of Er^{3+}: $^4I_{11/2}\rightarrow{}^4I_{13/2}$ is 109.5 s^{-1}, which is bigger than that of $Na_5Y_9F_{32}$ single crystal[48], fluorophosphate glasses (22.8 s^{-1})[43], oxyfluorotellurite glass (60.92 s^{-1})[10], and the fluorescence branching ratio β value of $^4I_{11/2}\rightarrow{}^4I_{13/2}$ reaches 14.9 %. Generally, the large values of the A_{ed}, A_{md}, and β indicate the probability of accomplishing strong 2.7 μm emissions.

3.3 Fluorescence analysis and energy transfer mechanism

During 500-700 nm, the up-conversion emission spectra of Er^{3+} ions doped, Er^{3+}/Pr^{3+} ions co-doped glass samples are demonstrated in **Fig. 4**. To provide comparative fluorescence emission data, the same experimental conditions were kept for each glass sample. For Er^{3+} single-doped samples, 544 nm and 664 nm bands were observed, which were related to Er^{3+}: $^2H_{11/2}$, $^4S_{3/2}\rightarrow{}^4I_{15/2}$ and Er^{3+}: $^4F_{9/2}\rightarrow{}^4I_{15/2}$ transition. As the concentration of Er^{3+} increased, the intensities of these bands became stronger.

For the Er^{3+}/Pr^{3+} ions co-doped GGSS glass samples, the up-conversion emission intensities decreased obviously as the concentration of Pr^{3+} increased, especially for the red up-conversion emission. The strong up-conversion emission is not advantageous to the implementation of the mid-infrared emission because they play the role of a competitive emission[43]. Therefore, the addition of Pr^{3+} ions helps to lower the negative up-conversion emission and consequently enhances mid-infrared fluorescence signals [49].

As presented in **Fig. 5**, by using a 980 nm laser, the infrared emission spectra were obtained in 1400-3000 nm. For Er^{3+} ions doped samples, the emission bands are mostly located on 1548 and 2736 nm, corresponding to Er^{3+}: $^4I_{13/2}\rightarrow{}^4I_{15/2}$ and Er^{3+}: $^4I_{11/2}\rightarrow{}^4I_{13/2}$ transitions. The peak of both bands became stronger and the intensity at 1548 nm increased several times stronger than that of 2736 nm as Er^{3+} concentration grew. For the co-doped samples, except for those bands mentioned above, a band at 1850 nm appeared according to the transition Pr^{3+}: $^3F_{3,4}\rightarrow{}^3H_4$. The intensity of this band first became stronger and then weakened with the increase of Pr^{3+} concentration. After co-doping with Pr^{3+}, the NIR emission intensity at 1548 nm became weak dramatically because the level of Er^{3+}: $^4I_{13/2}$ was quenched by Pr^{3+} via ET. While the increasing Pr^{3+} concentration initially increased the 2.7 μm fluorescent intensity and then became weak because of the excessive concentration of Pr^{3+}. This can be interpreted as when the concentration of Pr^{3+} increased, the distance between rare earth ions would become smaller and clusters of rare earth ions would form, which can improve the non-radiative relaxation probability and lower

fluorescence intensity[50]. The addition of Ga can certainly increase RE ions solubility because it allows for consistent RE ion separation when it forms the [RE^{3+}]-S-[Ga^{3+}] structure[51].

Fig. 6 is the electronic transitions schematic from Er^{3+} ions to Pr^{3+} ions, which can explain the fluorescence spectra mentioned above all. Excited by a 980 nm LD, the electrons on the $^4I_{15/2}$ level were pumped to the $^4I_{11/2}$ level, then the ETU1 (Energy cooperation upconversion) process: $^4I_{11/2} + {}^4I_{11/2} \rightarrow {}^4F_{7/2} + {}^4I_{15/2}$ happened. Electrons of $^4F_{7/2}$ level relaxed to the manifolds ($^2H_{11/2}$, $^4S_{3/2}$) and the level $^4F_{9/2}$ non-radiatively, then relaxed to ground level radiatively, thus generating 544 nm emission and 644 nm emission. Then, the electrons of the $^4I_{11/2}$ level underwent radiative decay to the $^4I_{13/2}$ level and after that, decayed to the $^4I_{15/2}$ level, thus generating 2.7 μm and 1.5 μm emission. At the same time, the ETU2: $^4I_{13/2} + {}^4I_{13/2} \rightarrow {}^4I_{9/2} + {}^4I_{15/2}$ occurred, deactivating the $^4I_{13/2}$ level, thus the electrons in the $^4I_{9/2}$ level quickly decayed to the $^4I_{11/2}$ level was advantageous to the emission of 2.7 μm[52].

After Pr^{3+} was introduced, the ET process of Er^{3+}: $^4I_{13/2}$ + Pr^{3+}: $^3H_4 \rightarrow Er^{3+}$: $^4I_{15/2}$ + Pr^{3+}: ($^3F_3$, $^3F_4$) (ET1) and Er^{3+}: $^4I_{11/2}$ + Pr^{3+}: $^3H_4 \rightarrow Er^{3+}$: $^4I_{15/2}$ + Pr^{3+}: $^1G_4$ (ET2) occurred without the assist of phonons because Er^{3+} and Pr^{3+} have adjacent energy levels. Therefore, the process of ET2 deactivated the Er^{3+}: $^4I_{11/2}$ level and restrained the up-conversion emission by directly weakening the ETU1 process. Meanwhile, the ET1 process can easily occur without the participation of phonons to deactivate the $^4I_{13/2}$ level, so it can decrease the 1.5 μm fluorescence intensity and improve the MIR fluorescence intensity of 2.7 μm. Undergoing the ET process, the electrons of Pr^{3+} ions were pumped to the excited state level, then relaxed through radiative and non-radiative transition, thus generating 1.8 μm emission.

The processes of ET1, ET2, and the phonon energy of glass all play roles in how Pr^{3+} affects a system. The efficiency of ET1 is much larger than ET2 owing to the oscillator strength of the former ET1 being so much higher than that of ET2, which causes electrons in the $^4I_{13/2}$ can radiate more dramatically than that of $^4I_{11/2}$, resulting in the possibility of population inversion as well as the enhancement of emission intensity at 2.7 μm.

3.4 Fluorescence decay analysis

As shown in **Figs. 7 (a)** and **7 (b)**, these GGSS glasses were used to gain the decay curves of the Er^{3+}: $^4I_{13/2}$ level and Er^{3+}: $^4I_{11/2}$ level, and the single exponential function was used to fit them,

$$I(t) = y_0 + A\exp(t/\tau) \quad (1)$$

where $I(t)$ is the emission intensity changed with time t, τ is the decay time, and A is a constant, respectively.

From **Fig. 7 (c)**, the lifetimes of Er^{3+}: $^4I_{13/2}$ level and Er^{3+}: $^4I_{11/2}$ levels were proportional to Er^{3+} concentration for Er^{3+} single-doped samples, except the $^4I_{11/2}$ energy level of 0.4 mol% Er^{3+} samples. It is observed in **Fig. 7 (d)** that after the introduction of Pr^{3+} ions, a rapid decrease from 7.33 ms to 1.90 ms was observed for $^4I_{13/2}$ levels lifetimes, while the lifetimes of $^4I_{11/2}$ levels reduced slightly from 2.01 ms to 1.40 ms as the concentration of Pr^{3+} increased, owing to the higher ET efficiency of ET1. Compared with the $^4I_{11/2}$ level, the reduction degree at the $^4I_{13/2}$ level was much higher, indicating that the Er^{3+}: $^4I_{13/2}$ level can be successfully quenched by Pr^{3+} ions via ET1 and ET2 processes. It is common knowledge that the Er^{3+} ion suffers the issue of "self-terminating", namely the $^4I_{13/2}$ level has a much longer lifetime in comparison to the $^4I_{11/2}$ level, so there are more electrons in the $^4I_{13/2}$ level. Pr^{3+} aids in dampening the self-termination effect, allowing the accumulated electrons at the $^4I_{13/2}$ level to relax quickly. With the appropriate Er^{3+}/Pr^{3+} doping concentration rate, it is possible to realize the population inversion to achieve efficient 2.7 μm laser output.

According to the measured lifetimes, the equation below was utilized to determine the efficiency of the energy transfer (η_{ET}) [53],

$$\eta_{ET} = 1 - \frac{\tau_{Pr/Er}}{\tau_{Er}} \quad (2)$$

where $\tau_{Pr/Er}$ and τ_{Er} are the measured lifetimes of Er^{3+} in the presence and absence of Pr^{3+} ions co-doping. From **Table 4**, for $0.2Er^{3+}/0.2Pr^{3+}$ glass, the η_{ET} of ET1 was up to 74%, much higher than that of ET2

(η_{ET2}=30%), indicating that the $^4I_{13/2}$ level can be easier depopulated than that of $^4I_{11/2}$, resulting in a possible population inversion.

3.5 Absorption cross sections, emission cross sections, and gain properties

For estimating the performance of the Er^{3+}/Pr^{3+} ions co-doped GGSS glasses as 2.7 μm laser materials, the emission and absorption cross section are vital values. The Füchtbauer-Ladenburg formula[54] was utilized to determine the emission cross-sections σ_e,

$$\sigma_e = \frac{A_{rad}\lambda^4}{8\pi c n^2} \times \frac{\lambda I(\lambda)}{\int \lambda I(\lambda) d\lambda} \quad (3)$$

where n is the refractive index of glass, A_{rad} presents the radiative transition probability of $^4I_{11/2} \rightarrow {}^4I_{13/2}$ and $I(\lambda)$ is the obtained emission intensity changed with wavelength λ.

Since the $^4I_{13/2}$ and $^4I_{11/2}$ both belong to the excited state level, their absorption spectra are hard to detect, thus the Mc-Cumber theory was used to calculate the absorption emission,

$$\sigma_e = \sigma_a \frac{Z_l}{Z_u} \exp\left(\frac{\varepsilon - hc\lambda^{-1}}{kT}\right) \quad (4)$$

where Z_l and Z_u represent the functions of lower to upper levels, k presents the Boltzmann constant, h presents the Planck constant, T presents the Kelvin temperature, and ε is the energy gap from the lowest Stark level of the ground state manifold to that of the upper manifold

Fig. 8 (a) presents the absorption and emission cross-sections of $0.2Er^{3+}/0.05Pr^{3+}$ GGSS glass at 2.7 μm. The σ_a of $^4I_{13/2} \rightarrow {}^4I_{11/2}$ is 0.933×10^{-20} cm^2 and the σ_e of $^4I_{11/2} \rightarrow {}^4I_{13/2}$ is 1.157×10^{-20} cm^2, and their FWHM is 137 nm and 132 nm, respectively. From **Table 4**, the σ_e of the Er^{3+}/Pr^{3+} co-doped GGSS glasses are all higher than 1.20×10^{-20} cm^2, which are bigger than that of fluorotellurite glass (0.90×10^{-20} cm^2)[55], B_2O_3-PbO-GeO_2-Bi_2O_3 glass (0.90×10^{-20} cm^2)[56], while smaller than that of GAGS glass (5.6×10^{-20} cm^2)[50]. A relatively big emission cross-section represents the probability of receiving more

laser gain, signifying that Er^{3+} and Pr^{3+} ions co-doped GGSS glass will be a competitive candidate as a 2.7 μm mid-infrared laser material.

For $0.2Er^{3+}/0.05Pr^{3+}$ GGSS glass, depending on the absorption cross-sections and emission cross-sections, the optical gain coefficients of Er^{3+}: $^4I_{11/2} \rightarrow {}^4I_{13/2}$ is calculated to estimate the emission ability of RE ion doped glass materials,

$$G(\lambda) = N P_e(\lambda) - (1-P)_a(\lambda) \quad (5)$$

where N is the doped concentration of RE ions, $\sigma_a(\lambda)$ and $\sigma_e(\lambda)$ are absorption and emission cross-sections, and P represents the electron population inversion ratio between different energy levels.

From **Fig. 8 (b)**, as the P value increase from 0 to 1, when $P \geqslant 0.4$, the gain coefficient will be positive, smaller than ZBLAN glass, indicating a low laser operation threshold. The maximum gain coefficient of Er^{3+}/Pr^{3+} co-doped GGSS glass is 0.85 cm^{-1}, which is higher than ZBLAN glass (0.6 cm^{-1})[57] and Ga_2S_3-GeS_2-CsCl glass (0.66 cm^{-1})[58]. Therefore, it is possible to obtain a strong 2.7 μm laser pulse with relatively small pump energy.

4. Conclusion

In conclusion, a progression of Er^{3+} and Pr^{3+} doped $Ga_5Ge_{20}Sb_{10}S_{65}$ glass samples were prepared, and then their basic physical performances were researched. The absorption spectra were collected, series of theoretical calculations were done consequently, obtaining the relative oscillator strengths of different transitions, and the high J-O parameters Ω_4/Ω_6 = 1.42, the large values of the radiative parameters A_{ed}, A_{md}, and β, all present the possibility of receiving strong 2.7 μm emission. Excited with a 980 nm laser, the emission intensity of up-conversion and 1.5 μm NIR reduced after the doping of Pr^{3+} ions, whereas the 2.7 μm mid-infrared emission improved when Er^{3+} and Pr^{3+} ions concentration ratio is proper, because the Er^{3+}: $^4I_{13/2}$ level can be effectively quenched via the ET process between Er^{3+} and Pr^{3+}. Meanwhile, the lifetimes of $^4I_{13/2}$ level for $0.2Er^{3+}/yPr^{3+}$ samples dropped dramatically from 7.33 ms to 1.90 ms when the concentration of Pr^{3+} increased, the decrease degree was much higher than

that of Er^{3+}: $^4I_{11/2}$, resulting in a possible population inversion. The corresponding ET efficiency of the $0.2Er^{3+}/0.2Pr^{3+}$ co-doped glasses reached 74%, which provided a feasibility to boost the weak MIR emission. The large value of the emission cross-sections of Er^{3+}: $^4I_{11/2}$ can exceed 10^{-20} cm^2, and the small pump energy was needed for the gain coefficients of Er^{3+}: $^4I_{11/2}\rightarrow{}^4I_{13/2}$, indicating the feasibility to obtain 2.7 μm MIR emission. The results show that the Er^{3+}/Pr^{3+} co-doped GGSS glass is a potential laser gain material for realizing 2.7 μm laser.

Acknowledgments

This work is financially supported by the National Natural Science Foundation of China (61975156, U2241236, 51876145)

References

[1] Bernier M, Michaudbelleau V, Levasseur S, Fortin V, Genest J, Vallée R. All-fiber DFB laser operating at 2.8 μm. Opt Lett. 2015;40(1):81-84.

[2] Zlatanovic S, Park JS, Moro S, Boggio JMC, Divliansky IB, Alic N*, et al.* Mid-infrared wavelength conversion in silicon waveguides using ultracompact telecom-band-derived pump source. Nat Photonics. 2010;4(8):561-564.

[3] Högele A, Hörbe G, Lubatschowski H, Welling H, Ertmerb W. 2.70 μm CrEr:YSGG laser with high output energy and FTIR-Q-switch. Opt Commun. 1996;125 (1-3):90-94.

[4] Seddon AB, Tang ZQ, Furniss D, Sujecki S, Benson T. Progress in rare-earth-doped mid-infrared fiber lasers. Opt Express. 2010;18(25):26704-26719

[5] Sujecki S, Sojka L, Pawlik E, Anders K, Piramidowicz R, Tang ZQ*, et al.* Numerical analysis of spontaneous mid-infrared light emission from terbium ion doped multimode chalcogenide fibers. J Lumin. 2018;199:112-115.

[6] Yang Y, Mei BC, Zhou ZW, Li WW, Sun ZC, Zhang YQ*, et al.* Fabrication and spectroscopic investigations on Er^{3+}, Ho^{3+}: SrF_2 transparent ceramics for 2.7 μm emission. J Eur Ceram Soc. 2021;42(4):1722-1730.

[7] Liu Z, She JB, Peng B. Spectroscopic properties of Er^{3+}-doped fluoroindate glasses. J Rare Earth. 2013;40(7):1037-1042.

[8] Li MH, Lei RS, Wang HP, Deng DG, Xu SQ. Preparation and optical properties of silver sensitized 6Y–ZrO_2: Er^{3+} translucent ceramics. Ceram Int. 2022;48(9):13386-13394.

[9] Huang FF, Ying T, Xu SQ, Zhang JJ. Spectroscopic and energy transfer mechanism of Er^{3+}, Pr^{3+} codoped ZBYA glass. Ceram Int. 2016;42(7):7924-7928.

[10] Bai GX, Ding J, Tao LL, Li KF, Hu LL, Tsang YH. Efficient 2.7 μm emission from Er^{3+}/Pr^{3+} co-doped oxyfluorotellurite glass. J Non-Cryst Solids. 2012;358(23):3403-3406.

[11] Zhou LF, Huang FF, Ren GY, Hua YJ, Lei RS, Xu SQ. Efficient Er^{3+}:$^4I_{11/2}\rightarrow{}^4I_{11/2}$ radiative transition regulated by optimizing the sensitization mechanism. Spectrochim Acta A. 2020;228:117853.

[12] Cheng P, Zhou Y, Su X, Zhou MH, Zhou ZZ, Shao HR. Pr^{3+}/Er^{3+} co-doped tellurite glass with ultra-broadband near-infrared fluorescence emission. J Lumin. 2018;197:31-37.

[13] He CJ, An Y, Deng CG, Gu XR, Wang JM, Wu T*, et al.* Tunable photoluminescent properties of rare-earth co-doped $(Na_{0.5}Bi_{0.5})TiO_3$ ceramics by Pr^{3+} concentration. Mod Phys Lett B. 2019;33(26): 1950323.

[14] Chen YZ, Zhang QL, He Y, Quan C, Luo JQ, Xu JY*, et al.* Diode end-pumped dual-wavelength Er,Pr:GSAG laser operating at 2696 and 2828 nm. Opt Laser Technol. 2020;121:105811.

[15] Sun ZD, Wang FF, Xia HP, Nie HK, Yang KJ, Wang RH*, et al.* Spectroscopic and laser properties of Er^{3+}, Pr^{3+} co-doped $LiYF_4$ crystal. Chin Opt Lett. 2021;19(8):081404.

[16] Meneghetti M, Caillaud C, Chahal R, Galdo E, Brilland L, Adam JL*, et al.* Purification of Ge-As-Se ternary glasses for the development of high quality microstructured optical fibers. J Non-Cryst Solids. 2019;503:84-88.

[17] Carcreff J, Masselin P, Boussard-Pledel C, Kulinski P, Troles J, Le Coq D. Step-index fibre from metal halide chalcogenide glasses. Opt Mater Express. 2020;10(11):2792-2804.

[18] Brown EE, Fleischman ZD, McKay J, Hommerich U, Palosz W, Trivedi S*, et al.* Spectroscopic study of Er-doped $Ga_2Ge_5S_{13}$ glass for mid-IR laser applications. Opt Mater Express. 2022;12(4):1627-1637.

[19] Ravagli A, Boetti NG, Cruz FAG, Alzaidy GA, Pugliese D, Milanese D*, et al.* Structural and spectral characterisation of Er^{3+} and Nd^{3+} doped Ga-La-S-Se glasses. RSC Adv. 2018;8(48):27556-27564.

[20] Ari J, Starecki F, Boussard-Pledel C, Ledemi Y, Messaddeq Y, Doualan JL*, et al.* Co-doped Dy^{3+} and Pr^{3+} $Ga_5Ge_{20}Sb_{10}S_{65}$ fibers for mid-infrared broad emission. Opt Lett. 2018;43(12):2893-2896.

[21] Lucas P, Coleman GJ, Sen S, Cui S, Guimond Y, Calvez L*, et al.* Structural and chemical homogeneity of chalcogenide glass prepared by melt-rocking. J Chem Phys. 2019;150(1):014505.

[22] Starecki F, Abdellaoui N, Braud A, Doualan JL, Boussard-Pledel C, Bureau B*, et al.* 8 μm luminescence from a Tb^{3+} GaGeSbSe fiber. Opt Lett. 2018;43(6):1211-1214.

[23] Crane RW, Sojka L, Furniss D, Nunes J, Barney E, Farries MC, *et al.* Experimental photoluminescence and lifetimes at wavelengths including beyond 7 μm in Sm^{3+} doped selenide-chalcogenide glass fibers. Opt Express. 2020;28(8):12373-12384.

[24] Chahal R, Starecki F, Doualan JL, Němec P, Trapananti A, Prestipino C*, et al.* Nd^{3+}:Ga-Ge-Sb-S glasses and fibers for luminescence in mid-IR: synthesis, structural characterization and rare earth spectroscopy. Opt Mater Express. 2018;8(6):1650-1671.

[25] Ma CC, Guo HT, Xu YS, Wu ZH, Li MM, Jia XM*, et al.* Effect of glass composition on the physical properties and luminescence of Pr^{3+} ion doped chalcogenide glasses. J Am Ceram Soc. 2019;102 (11):6794-6801.

[26] Charpentier F, Starecki F, Doualan JL, Jóvári P, Camy P, Troles J*, et al.* Mid-IR luminescence of Dy^{3+} and Pr^{3+} doped $Ga_5Ge_{20}Sb_{10}S(Se)_{65}$ bulk glasses and fibers. Mater Lett. 2013;101(5):21-24.

[27] Lucovsky G, Deneufville JP, Galeener FL. Study of the optic modes of $Ge_{0.30}S_{0.70}$ glass by infrared and Raman spectroscopy. Phys Rev B 1974;9(4):1591-1597.

[28] Pangavhane SD, Němec P, Nazabal V, Moreac A, Jovari P, Havel J. Laser desorption ionization time-of-flight mass spectrometry of Erbium-doped Ga-Ge-Sb-S Glasses. Rapid Commun Mass Sp. 2014;28(11):1221-1232.

[29] Sugai. Stochastic random network model in Ge and Si chalcogenide glasses. Phys Rev B. 1987;35(3):1345-1361.

[30] Guignard M, Nazabal V, Smektala F, Adam JL, Bohnke O, Duverger C*, et al.* Chalcogenide glasses based on germanium disulfide for second harmonic generation. Adv Funct Mater. 2007;17(16):3284-3294.

[31] Fabian M, Svab E, Pamukchieva V, Szekeres A, Todorova K, Vogel S*, et al.* Reverse Monte Carlo modeling of the neutron and X-ray diffraction data for new chalcogenide Ge–Sb–S(Se)–Te glasses. J Phys Chem Solids. 2013;74(10):1355-1362.

[32] Kadono K, Takahashi M, Higuchi H, Shojiya M, Peyghambarian N. Frequency upconversion of Er^{3+} in Ga_2S_3-GeS_2-La_2S_3 glasses. Proc SPIE. 1997;2996:25-31.

[33] Li MM, Xu YS, Jia XM, Yang L, Long NB, Liu ZJ*, et al.* Mid-infrared emission properties of Pr^{3+}-doped Ge-Sb-Se-Ga-I chalcogenide glasses. Opt Mater Express. 2018;8(4):1617-1622.

[34] de Sousa DF, Sampaio JA, Nunes L, Baesso ML, Bento AC, Miranda L. Energy transfer and the 2.8 μm emission of Er^{3+}- and Yb^{3+}-doped low silica content calcium aluminate glasses. Phys Rev B. 2000;62(5):3176-3180.

[35] Pecoraro E, de Sousa DF, Lebullenger R, Hernandes AC, Nunes L. Evaluation of the energy transfer rate for the Yb^{3+}: Pr^{3+} system in lead fluoroindogallate glasses. J Appl Phys. 1999;86(6):3144-3148.

[36] Judd BR. Optical absorption intensities of Rare-Earth ions. Phys Rev B. 1962;127(3):750-761.

[37] Librantz AFH, Jackson SD, Gomes L, Ribeiro SJL, Messaddeq Y. Pump excited state absorption in holmium-doped fluoride glass. J Appl Phys. 2008;103(2):023105.

[38] Stefan Kuhn, Herrmann Andreas, Rüssel C. Judd–Ofelt analysis of Sm^{3+}-doped lanthanum-aluminosilicate glasses. J Lumin. 2015;157:390-397.

[39] Sugimoto N, Kuroiwa Y, Ito S. Broad-band 1.5 μm emission of Er^{3+} ions in bismuth-based oxide glasses for potential WDM amplier. J Lumin. 2000;87:670-672.

[40] Moizan V, Nazabal V, Troles J, Houizot P, Adam JL, Doualan JL*, et al.* Er^{3+}-doped GeGaSbS glasses for mid-IR fibre laser application: Synthesis and rare earth spectroscopy. Opt Mater. 2009;31(1):39-46.

[41] Christian K, Jorgensen, Reisfeld R. Judd-Ofelt parameters and chemical bonding. Journal of the Less-Common Metals. 1983;93(1):107-112.

[42] Carnall WT, Fields PR, Rajnak K. Electronic Energy Levels in the Trivalent Lanthanide Aquo Ions. I. Pr^{3+}, Nd^{3+}, Pm^{3+}, Sm^{3+}, Dy^{3+}, Ho^{3+}, Er^{3+}, and Tm^{3+}. J Chem Phys. 1968;49(10):4424-4442.

[43] Zhang LY, Xue TF. Discrepancies between Pr^{3+} and Ho^{3+} de-sensitized Er^{3+}: 2.7μm emission. J Lumin. 2016;178:22-26.

[44] Cheng P, Zhou X, Su X, Zhou MH, Zhou ZZ, Shao HR. Pr^{3+}/Er^{3+} co-doped tellurite glass with ultra-broadband near-infrared fluorescence emission. J Lumin. 2018;197:31-37.

[45] Choi YG, Kim KH, Lee BJ, Shin YB, Kim YS, Heo J. Emission properties of the Er^{3+}: $^4I_{11/2}\rightarrow{}^4I_{13/2}$ transition in Er^{3+} and Er^{3+}/Tm^{3+} doped Ge-Ga-As-S glasses. J Non-Cryst Solids. 2000;278(1-3):137-144.

[46] Ofelt GS. Intensities of Crystal Spectra of Rare-Earth Ions. J Chem Phys. 1962;37(3):511-520.

[47] Krupke WF, Gruber JB. Optical-Absorption Intensities of Rare-Earth Ions in Crystals: the Absorption Spectrum of Thulium Ethyl Sulfate. Phys Rev. 1965;139(6A):A2008-A2016.

[48] Qiao Y, Zhou X, Zhang JL, Xia HP, Song HW, Chen BJ. Enhanced mid-infrared emissions of Ho^{3+}/Er^{3+} co-doped $Na_5Y_9F_{32}$ single crystal by introduction of Pr^{3+} ions. J Alloy Compd. 2020;824:153987.

[49] Liu YY, Sun YJ, Wang Y, You ZY, Zhu ZJ, Li JF*, et al.* Benefit of Nd^{3+} ions to the ~2.7 μm emission of Er^{3+}: $^4I_{11/2}\rightarrow{}^4I_{13/2}$ transition in Nd,Er: $CaLaGa_3O_7$ laser crystal. J Lumin. 2018;198:40-45.

[50] Gan HT, Liu ZJ, Xia KL, Zhang XS, Gui YM, Dai SX. Er^{3+}/Pr^{3+} co-doped GeAsGaSe chalcogenide glasses for infrared emissions and their potential in 2.7 μm fiber laser. Ceram Int. 2020;46(18):28125-28131.

[51] Shiryaev VS, Velmuzhov AP, Tang ZQ, Churbanov MF, Seddon AB. Preparation of high purity glasses in the Ga–Ge–As–Se system. Opt Mater. 2014;37:18-23.

[52] Jackson SD, Pollnau M, Li JF. Diode pumped Erbium cascade fiber lasers. IEEE J Quantum Elect. 2011;47(4):471-478.

[53] Chen JK, Sun DL, Luo JQ, Zhang HL, Dou RQ, Xiao JZ*, et al.* Spectroscopic properties and diode

end-pumped 2.79 μm laser performance of Er, Pr: GYSGG crystal. Opt Express. 2013;21(20):23425-23432.

[54] Wang Y, Li JF, Zhu ZJ, You ZY, Tu C. Activation effect of Ho^{3+} at 2.84 μm MIR luminescence by Yb^{3+} ions in GGG crystal. Opt Lett. 2013;38(20):3988-3890.

[55] Zhou B, Tao LL, Tsang YH, Jin W, Pun EYB. Superbroadband near-infrared emission and energy transfer in Pr^{3+}-Er^{3+} codoped fluorotellurite glasses. Opt Express. 2012;20(11):12205-12211.

[56] Herrera A, Jacinto. C, Becerra AR, Franzen PL, Balzarettia NM. Multichannel emission from Pr^{3+} doped heavy-metal oxide glass B_2O_3-PbO-GeO_2-Bi_2O_3 for broadband signal amplification. J Lumin. 2016;180:341-347.

[57] Wang B, Cheng LH, Zhong HY, Sun JS, Tian Y, Zhang XQ*, et al.* Excited state absorption cross sections of $^4I_{13/2}$ of Er^{3+} in ZBLAN. Opt Mater. 2009;31(11):1658-1662.

[58] Hang L, Chen D, Yu Y, Yang A, Wang Y. Enhanced mid-infrared emissions of Er^{3+} at 2.7 μm via Nd^{3+} sensitization in chalcohalide glass. Opt Lett. 2011;36(10):1815-1817.

Figure caption list：

Fig. 1 (a) XRD patterns of Er^{3+} ions doped glass samples. (b) DSC curve of GGSS matrix glass. (c) Transmission spectrum of GGSS bulk glass. Inset shows the image of the glass. (d) Refractive indices curves of GGSS-0.2Er^{3+}/$x$$Pr^{3+}$ (x = 0, 0.05, 0.1, 0.2, mol%) and the inset presents the density change of those glasses.

Fig. 2 Deconvolution of Raman spectrum of the GGSS bulk glass using Gaussian fitting.

Fig. 3 (a) Absorption coefficients of different Er^{3+} doped GGSS glass samples. (b) Integrated area of the 980 nm absorption bands as Er^{3+} increases. (c) Absorption coefficients of Er^{3+} ions doped, Pr^{3+} ions doped, Er^{3+}/Pr^{3+} ions co-doped glass samples.

Fig. 4 Up-conversion emission spectra of (a) GGSS-$x$$Er^{3+}$, (b) GGSS-0.05$Er^{3+}$/$y$$Pr^{3+}$, (c) GGSS-0.1$Er^{3+}$/$y$$Pr^{3+}$ and (d) GGSS-0.2Er^{3+}/$y$$Pr^{3+}$ glass samples at 500-700 nm.

Fig. 5 Measured infrared emission spectra of (a) GGSS-$x$$Er^{3+}$, (b) GGSS-0.05$Er^{3+}$/$y$$Pr^{3+}$, (c) GGSS-0.1$Er^{3+}$/$y$$Pr^{3+}$ and (d) GGSS-0.2Er^{3+}/$y$$Pr^{3+}$ glass samples at 1400-3000 nm.

Fig. 6 Energy transfer mechanisms of Er^{3+}/Pr^{3+} ions co-doped GGSS glasses.

Fig. 7 The decay curves of Er^{3+}/Pr^{3+} ions co-doped GGSS glasses measured at (a) 1.5 μm and (b) 2.7 μm. Measured lifetimes results of $^4I_{13/2}$ level and $^4I_{11/2}$ level for (c) Er^{3+} ions single-doped glasses, (d) Er^{3+}/Pr^{3+} ions co-doped samples.

Fig. 8 (a) Absorption and emission cross-sections for GGSS-0.2Er^{3+}/0.05Pr^{3+} glass at 2.7 μm. (b) Calculated gain coefficients related to the $^4I_{11/2}$→$^4I_{13/2}$ of 0.2Er^{3+}/0.05Pr^{3+} GGSS glass.

Table caption list

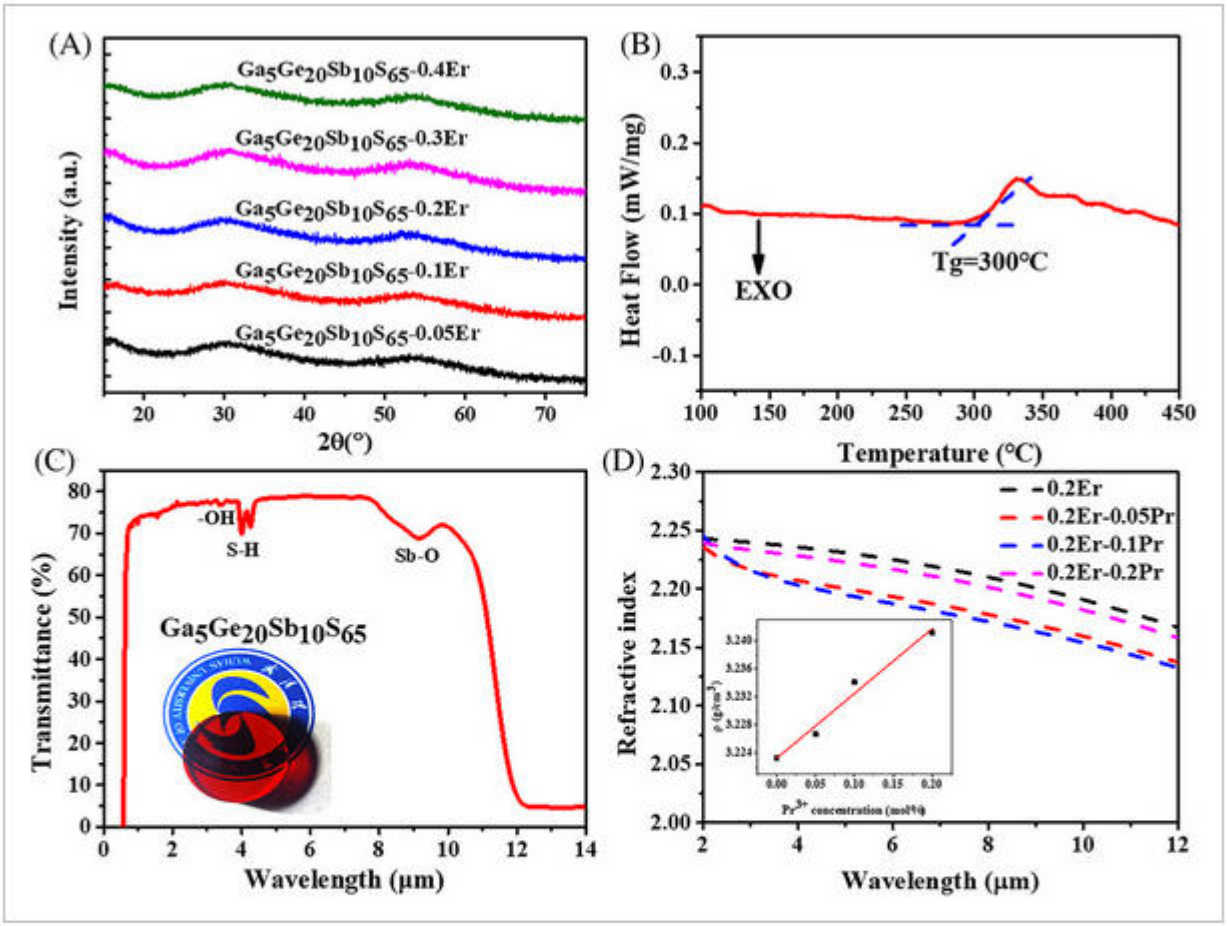

FIGURE 1

Open in figure viewer | PowerPoint

(A) X-ray diffractometer (XRD) patterns of Er^{3+} ions doped glass samples; (B) differential scanning calorimeter (DSC) curve of GGSS matrix glass; (C) transmission spectrum of GGSS bulk glass. Inset shows the image of the glass; (d) refractive indices curves of GGSS–$0.2Er^{3+}$/xPr^{3+} (x = 0, 0.05, 0.1, and 0.2, mol%) and the inset present the density change of those glasses.

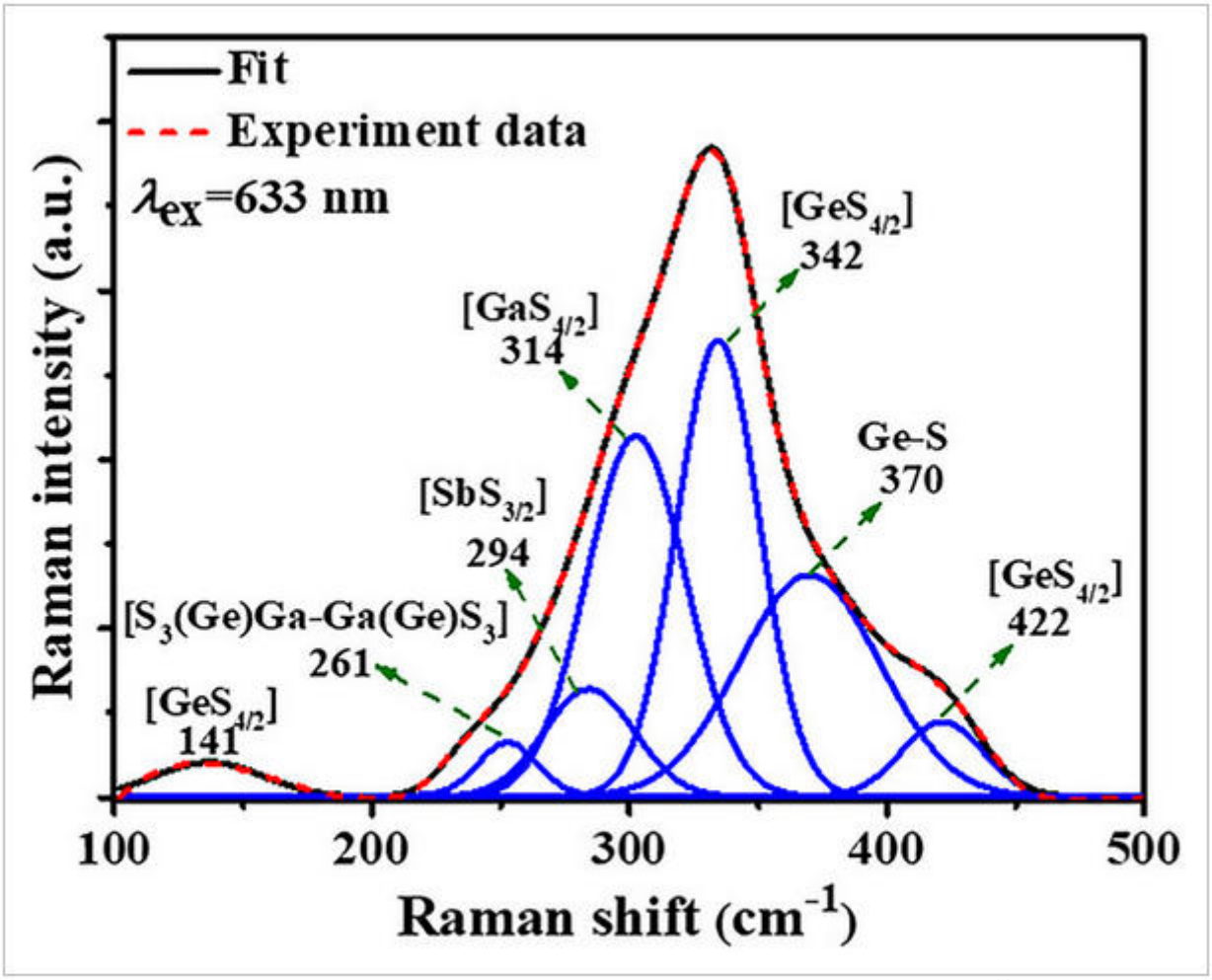

FIGURE 2

Open in figure viewer | PowerPoint

Deconvolution of Raman spectrum of the GGSS bulk glass using Gaussian fitting.

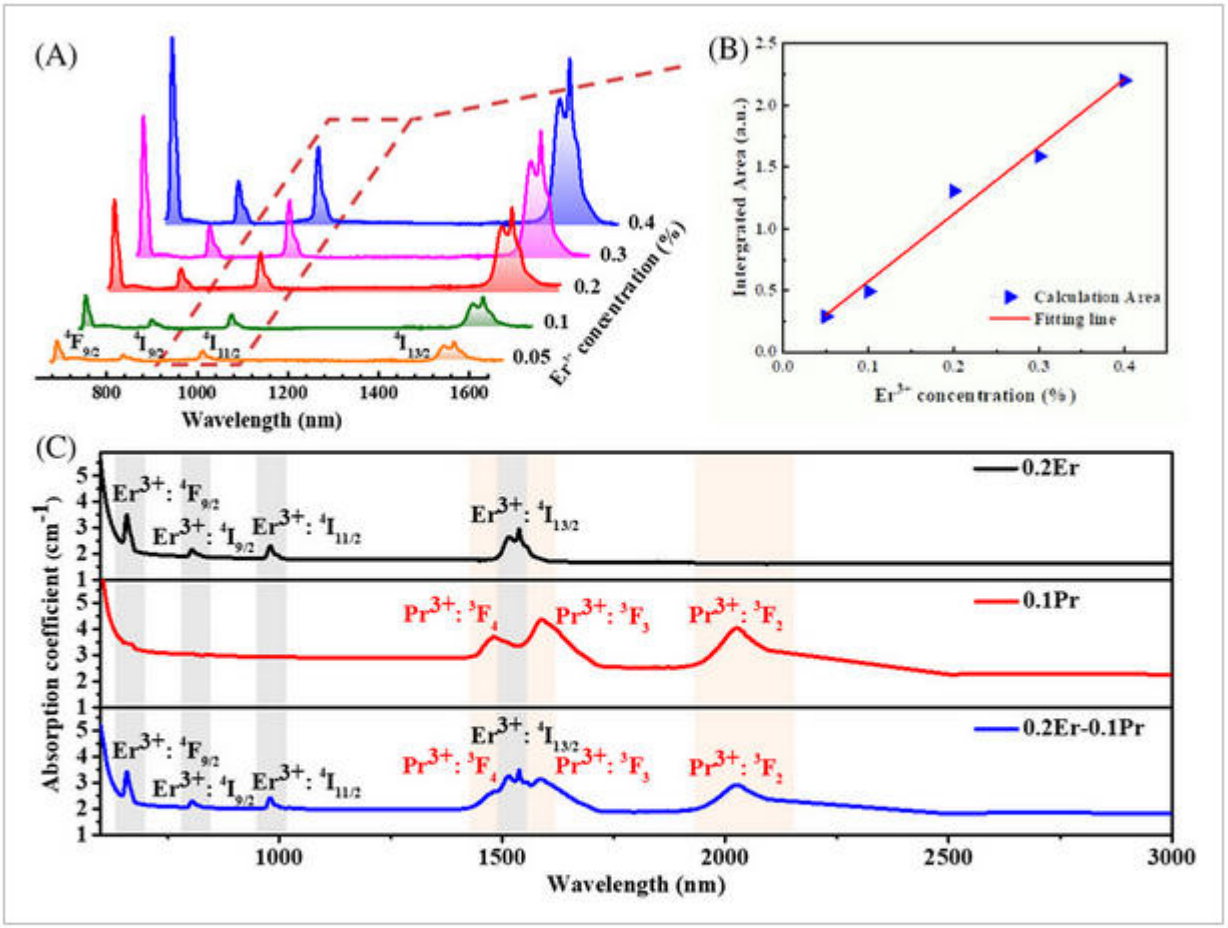

FIGURE 3

Open in figure viewer | PowerPoint

(A) Absorption coefficients of different Er^{3+} doped GGSS glass samples; (B) integrated area of the 980 nm absorption bands as Er^{3+} increases; (C) absorption coefficients of Er^{3+} ions doped, Pr^{3+} ions doped, and Er^{3+}/Pr^{3+} ions co-doped glass samples.

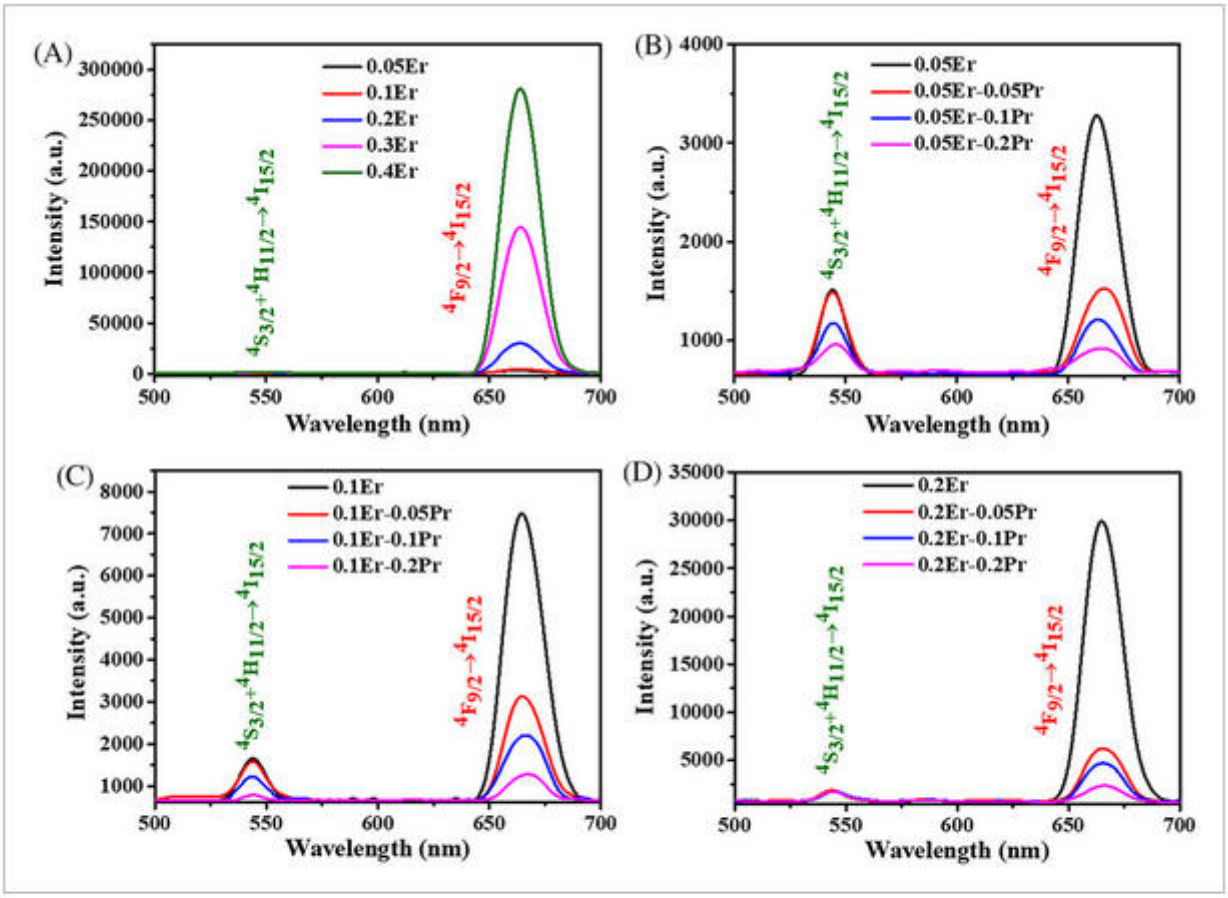

FIGURE 4

Open in figure viewer | PowerPoint

Up-conversion emission spectra of (A) GGSS–xEr^{3+}, (B) GGSS–0.05Er^{3+}/yPr^{3+}, (C) GGSS–0.1Er^{3+}/yPr^{3+}, and (D) GGSS–0.2Er^{3+}/yPr^{3+} glass samples at 500–700 nm.

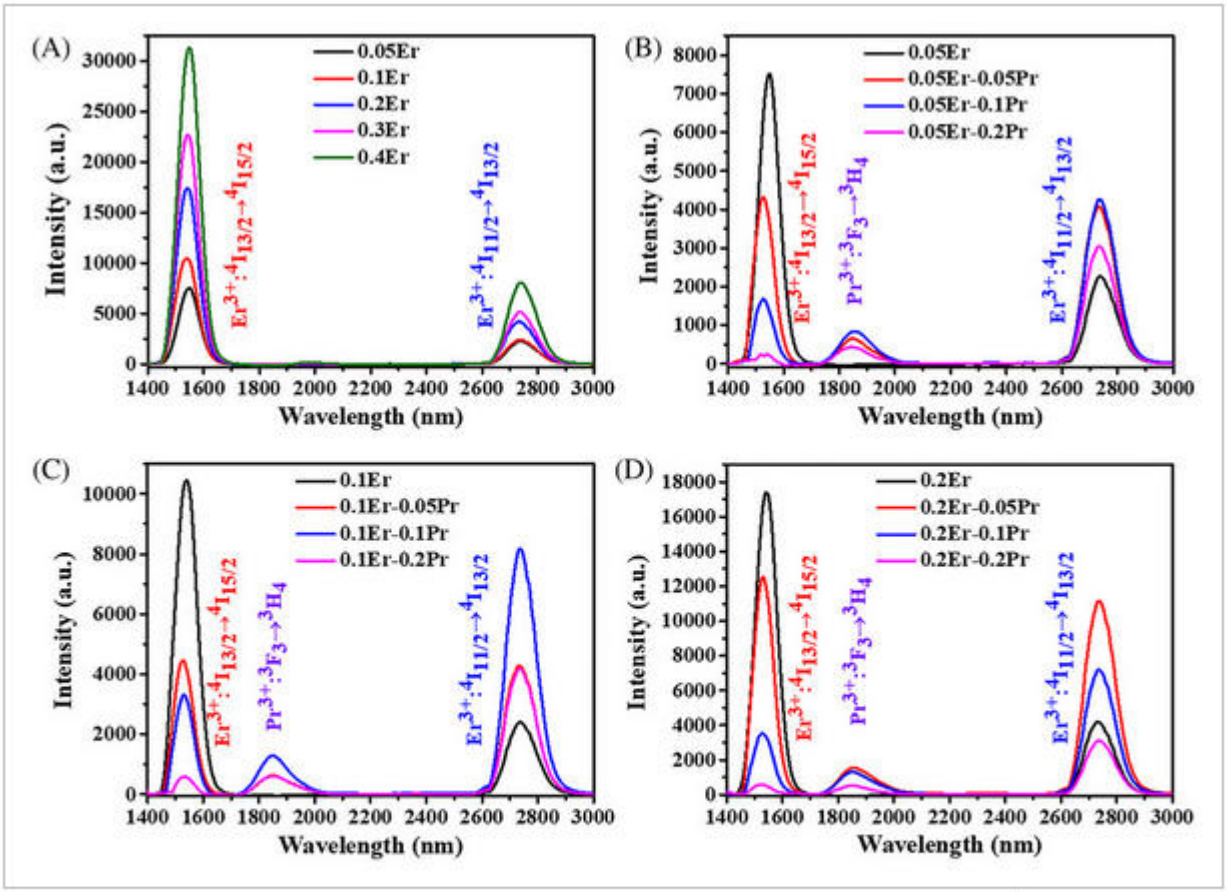

FIGURE 5

Open in figure viewer | PowerPoint

Measured infrared emission spectra of (A) GGSS–xEr^{3+}, (B) GGSS–0.05Er^{3+}/yPr^{3+}, (C) GGSS–0.1Er^{3+}/yPr^{3+}, and (D) GGSS–0.2Er^{3+}/yPr^{3+} glass samples at 1400–3000 nm.

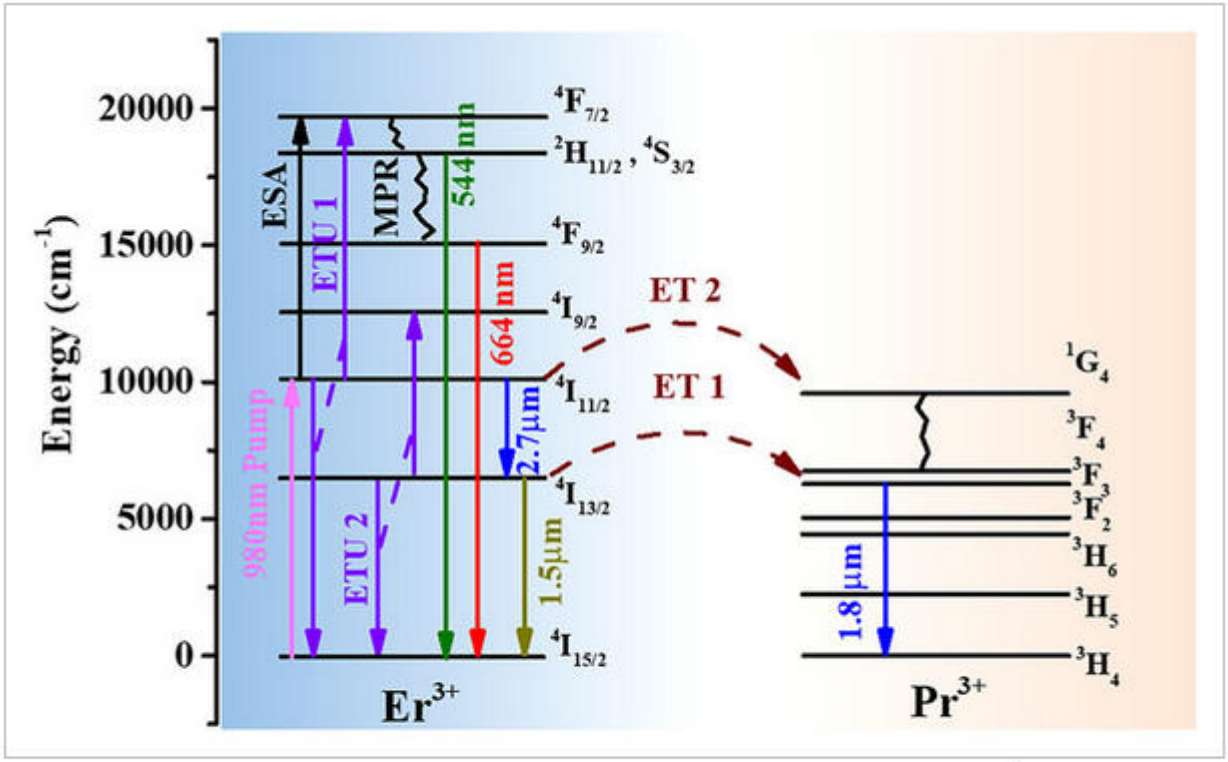

FIGURE 6

Open in figure viewer | PowerPoint

Energy transfer mechanisms of Er^{3+}/Pr^{3+} ions co-doped GGSS glasses.

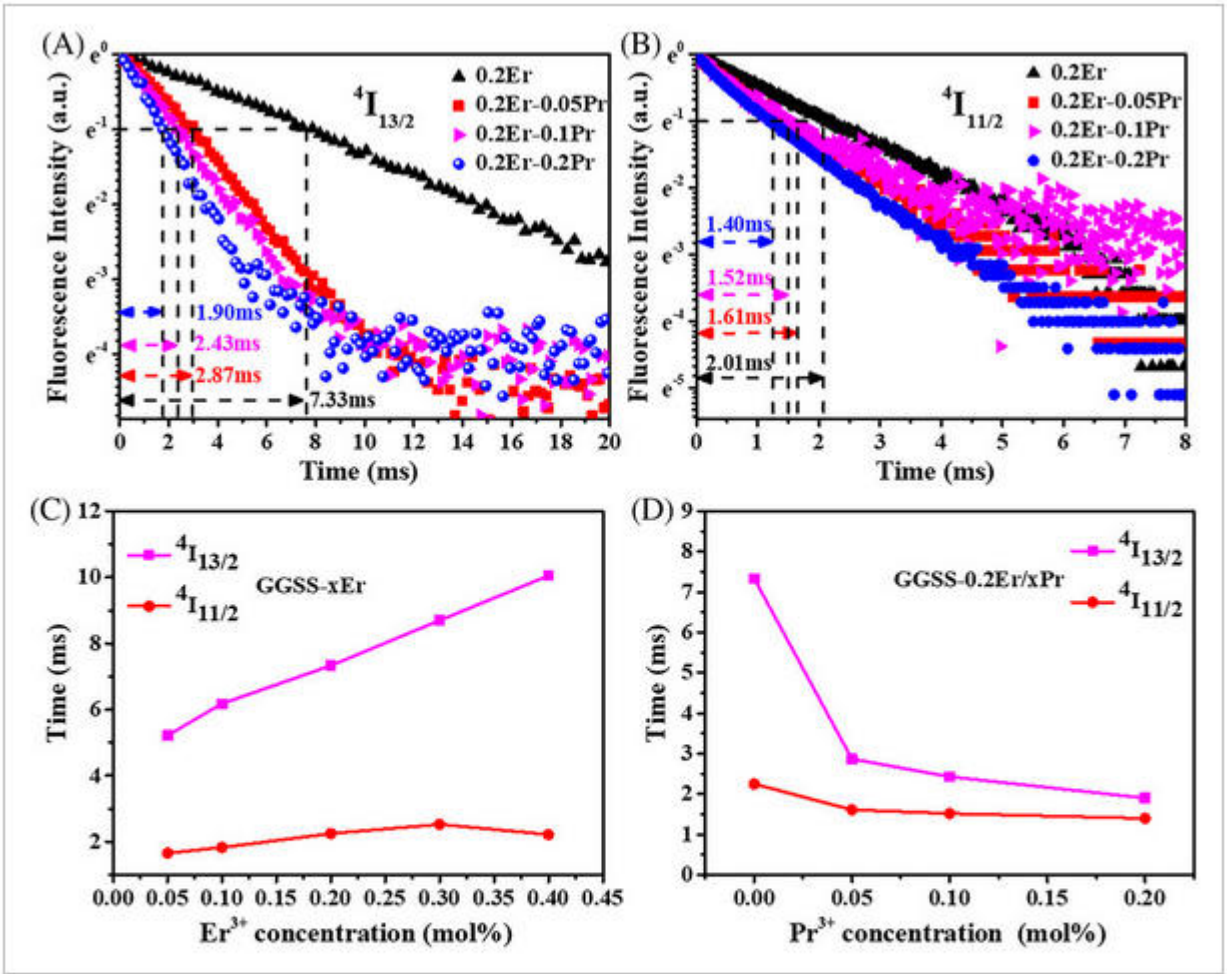

FIGURE 7

Open in figure viewer | PowerPoint

The decay curves of Er^{3+}/Pr^{3+} ions co-doped GGSS glasses measured at (A) 1.5 μm and (B) 2.7 μm. Measured lifetimes results of $^4I_{13/2}$ level and $^4I_{11/2}$ level for (C) Er^{3+} ions single-doped glasses, (D) Er^{3+}/Pr^{3+} ions co-doped samples.

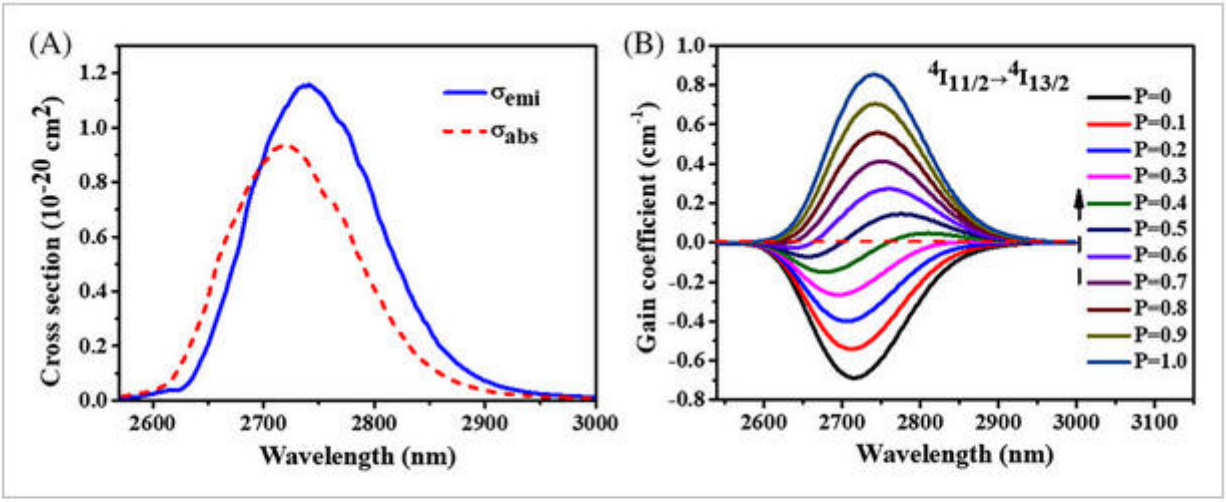

FIGURE 8

Open in figure viewer | PowerPoint

(A) Absorption and emission cross sections for GGSS–0.2Er^{3+}/0.05Pr^{3+} glass at 2.7 μm; (B) calculated gain coefficients related to the $^4I_{11/2} \rightarrow {}^4_{13/2}$ of 0.2Er^{3+}/0.05Pr^{3+} GGSS glass.

Table 1 The experimental (f_{exp}) and calculated (f_{cal}) oscillator strengths of transitions of the GGSS-0.2Er^{3+} glass

Table 2 J-O parameters Ω_t (t = 2, 4, 6) for Er^{3+} in different glasses

Table 3 The calculated transition probability of electrical dipole (A_{ed}), magnetic dipole (A_{md}), total radiative probabilities (A_{rad}), fluorescence branching ratio (β), and radiative lifetime (τ_{rad}) of the prepared glasses

Table 4 The absorption, emission cross-section, and lifetimes energy transfer efficiency of different GGSS glasses

Table 1 The experimental (f_{exp}) and calculated (f_{cal}) oscillator strengths of transitions of the GGSS-0.2Er^{3+} glass

transitions	wavelength (nm)	oscillator strength ($\times 10^{-6}$)	
		f_{exp}	f_{cal}
$^4I_{13/2} \rightarrow {}^4I_{15/2}$	1535	3.603	3.633
$^4I_{11/2} \rightarrow {}^4I_{15/2}$	981	1.196	1.111
$^4I_{9/2} \rightarrow {}^4I_{15/2}$	809	0.897	0.784
$^4F_{9/2} \rightarrow {}^4I_{15/2}$	641	5.486	5.463

Table 2 J-O parameters Ω_t (t = 2, 4, 6) for Er^{3+} in different glasses

matrix	Ω_t ($\times 10^{-20}$ $cm^{2)}$			Ω_4/Ω_6	Ref.
	Ω_2	Ω_4	Ω_6		
ZBYA	3.74	1.78	1.50	1.19	[9]
Oxyfluorotellurite glass	5.40	2.00	1.35	1.48	[10]
Fluorophosphate glass	5.14	1.02	0.91	1.12	[43]

Tellurite glass	5.68	1.20	1.82	0.66	[44]
Se-GLS glass	2.22	9.31	9.31	1.00	[19]
$Ge_{30}Ga_2As_6S_{62}$	6.93	2.18	0.87	2.51	[45]
$Ga_5Ge_{20}Sb_{10}S_{65}$ glass	8.62	2.44	1.72	1.42	This work

Table 3 The calculated transition probability of electrical dipole (A_{ed}), magnetic dipole (A_{md}), total radiative probabilities (A_{rad}), fluorescence branching ratio (β), and radiative lifetime (τ_{rad}) of the prepared glasses

Transition	ΔE (cm^{-1})	λ_p (nm)	A_{ed} (s^{-1})	A_{md} (s^{-1})	A_{rad} (s^{-1})	β (%)	τ_{rad} (ms)
$^4I_{13/2}\rightarrow{}^4I_{15/2}$	6514.7	1535	374.1	87.2	461.3	100	2.167
$^4I_{11/2}\rightarrow{}^4I_{15/2}$	10214.5	979	625.6	–	625.6	85.1	1.274
$^4I_{11/2}\rightarrow{}^4I_{13/2}$	3654.9	2736	82.4	27.1	109.5	14.9	–
$^4I_{9/2}\rightarrow{}^4I_{15/2}$	12473.8	804	732.9	–	732.9	81.4	1.062
$^4F_{9/2}\rightarrow{}^4I_{15/2}$	15197.6	658	5247.1	–	5247.1	92.6	0.143
$^4S_{3/2}\rightarrow{}^4I_{15/2}$	18382.4	544	1612.5	–	1612.5	61.3	0.354

Table 4 The absorption, emission cross-section, and lifetimes energy transfer efficiency of different GGSS glasses

Glass	σ_a @980 (10^{-20} cm)	σ_e, $^4I_{11/2}$ (10^{-20} cm^2)	$\sigma_e\tau$ ($^4I_{11/2}$) (10^{-23} cm^2·s)	Er^{3+}: $^4I_{13/2}$		Er^{3+}: $^4I_{11/2}$	
				τ_m (ms)	η_{ET1}	τ_m (ms)	η_{ET2}
$0.05Er^{3+}$	7.901	1.215	2.016	5.22	/	1.66	/
$0.1Er^{3+}$	4.436	1.207	2.184	6.18	/	1.83	/
$0.2Er^{3+}$	2.726	1.213	2.730	7.33	/	2.01	/
$0.3Er^{3+}$	2.077	1.233	3.118	8.70	/	2.53	/
$0.4Er^{3+}$	1.661	1.246	2.766	10.04	/	2.22	/
$0.2Er^{3+}/0.05Pr^{3+}$	2.846	1.157	2.023	2.87	60.85%	1.61	19.90%
$0.2Er^{3+}/0.1Pr^{3+}$	3.117	1.163	1.920	2.43	66.85%	1.52	24.38%
$0.2Er^{3+}/0.2Pr^{3+}$	2.962	1.179	1.791	1.90	74.08%	1.40	30.35%